Pneumatic Control of Robots for Rehabilitation

Eric T. Wolbrecht, David J. Reinkensmeyer and James E. Bobrow

The International Journal of Robotics Research 2010 29: 23 originally published online 19 May 2009
DOI: 10.1177/0278364909103787

Eric T. Wolbrecht
Mechanical Engineering Department,
University of Idaho,
Moscow, ID 83844,
USA
ewolbrec@uidaho.edu

David J. Reinkensmeyer
Mechanical and Aerospace and
Biomedical Engineering Departments,
University of California,
Irvine, CA 92697,
USA
dreinken@uci.edu

James E. Bobrow
Mechanical and Aerospace Engineering Department,
University of California,
Irvine, CA 92697,
USA
jebobrow@uci.edu

Pneumatic Control of Robots for Rehabilitation

Abstract

Pneumatic actuators are attractive for robotic rehabilitation applications because they are lightweight, powerful, and compliant, but their control has historically been difficult, limiting their use. In this paper we present the pneumatic control system developed for Pneu-WREX: a pneumatically actuated, upper extremity orthosis for rehabilitation after stroke. The developed pneumatic control system combines several novel components to make the entire system stable, reliable, and backdrivable. These components, which are described in this paper, include: (1) a unique two-valve force control subsystem that keeps chamber pressure low (to reduce friction and energy consumption) and adaptively compensates for leakage; (2) a new servovalve characterization approach that uses experimentally measured data in a combined non-linear and least-squares regression to obtain a linear relationship between mass flow and valve voltage; and (3) a new approach to state estimation using accelerometers and a Kalman filter to obtain clean signals for use in a non-linear adaptive feedback control law. Experimental testing of the device demonstrates the efficacy of the developed pneumatic control system.

KEY WORDS—neurorehabilitation, kalman filter, state estimation, Lyapunov's direct method, nonlinear control, force control, pneumatic control, compliance, movement training, servovalve characterization, radial basis functions, impairment modeling

1. Introduction

The goals for a rehabilitation robot are significantly different to those of a typical industrial robot. A robotic movement training device for people recovering after stroke or other neurological impairments would ideally be simultaneously strong and compliant, able to assist a subject in completing movements while remaining compliant so that the subject can see the effects of their effort. Therefore, the traditional challenges for an industrial robotic device, high accuracy, high mechanical stiffness, and high bandwidth, are supplanted by the challenges specific to rehabilitation robotics, light weight, high strength, and low impedance. Although control challenges have limited their application in the past, pneumatic actuators can potentially meet the requirements of rehabilitation robots because they have a high power-to-weight ratio, are mechanically compliant because of the inherent compliance of air, and

The International Journal of Robotics Research
Vol. 29, No. 1, January 2010, pp. 23–38
DOI: 10.1177/0278364909103787

Figures 1, 5, 6, 8–10, 12–15, 17 appear in color online: http://ijr.sagepub.com

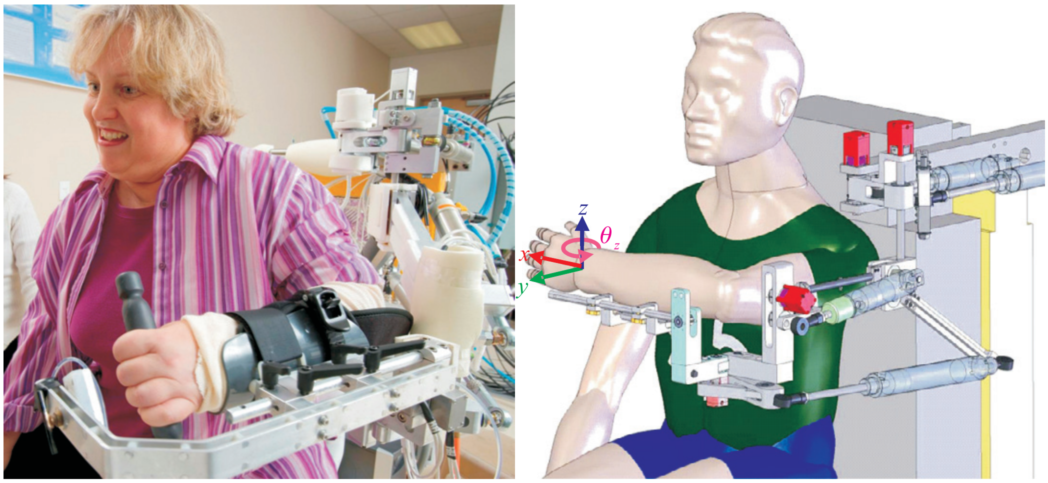

Fig. 1. Pneu-WREX: a four degree-of-freedom pneumatically actuated upper extremity orthosis for robotic movement training. The robot controls the position of the hand grip sensor. A forearm cuff provides additional support. The robot can translate freely along all three axes, but is constrained to only allow rotation about the z-axis. Specific kinematics are given in Appendix A.

are force controllable. They also have some disadvantages, including non-linearities in both force and airflow dynamics, and the requirement of an external source of compressed air.

The control of pneumatic cylinders is well documented in the literature, with primary methods including feedback linearization (Bobrow and McDonell 1998; Xiang and Wikander 2004) and sliding mode control (Surgenor and Vaughan 1997; Richer and Hurmuzlu 2000a,b; Fite et al. 2006). These methods typically included servovalve airflow modeling, either from experimental data (Bobrow and McDonell 1998; Leavitt et al. 2006; Wolbrecht et al. 2006) or using nozzle flow equations (Shearer 1956; Richer and Hurmuzlu 2000a,b; Xiang and Wikander 2004). Some of the existing pneumatic movement training devices, notably the RUPERT upper extremity movement devices (He et al. 2005), use open-loop control. Other pneumatic robotic movement training devices, notably the PAM/POGO gait training system (Reinkensmeyer et al. 2006), use a hierarchical control scheme where low-level force control uses feedback linearization or sliding mode control and the higher-level, outer-loop control uses conventional control schemes such as PD control.

A general adaptive, model-based "assist-as-needed' control architecture developed for Pneu-WREX (Wilmington Robotic Exoskeleton (Rahman et al. 2004), see Figure 1) is described in Wolbrecht et al. (2008) and further details are given in Appendix A. This general control architecture can be applied to any robot (electric or pneumatic) and the steps necessary for its implementation on a low-cost pneumatically actuated robot have not been presented previously. Here we demonstrate that our control architecture, as applied to Pneu-WREX, achieves good results appropriate for robotic movement training. Our approach requires the development of a novel Kalman filter for state estimation, inclusion of flow dynamics of air and leakage estimation in the Lyapunov analysis, servovalve characterization using experimental data, and an adaptive model of a patient's abilities and effort. These components are described in the following sections.

2. Adaptive Position Controller

Pneu-WREX uses a model-based adaptive controller for position control during robotic movement training. The use of model-based control allows the interaction between the device and human subject to remain compliant while also providing sufficient force to assist even severely impaired subjects in completing movements. The adaptive part of the controller allows it to learn as the ability of each person who has suffered a stroke varies. This is necessary because the impairment level varies widely from subject to subject.

The adaptive position controller includes the "position control subsystem" and "state estimation subsystem" shown in Figure 2. These subsystems, along with the combined orthosis and arm dynamics, are described in the following sections.

2.1. Combined Orthosis and Arm Dynamics

The rigid body dynamics of a robotic orthosis when connected to a human subject are defined in task coordinates as

$$\mathbf{M}(\mathbf{x})\,\ddot{\mathbf{x}} + \mathbf{C}(\mathbf{x},\dot{\mathbf{x}})\,\dot{\mathbf{x}} + \mathbf{N}(\mathbf{x},\dot{\mathbf{x}}) = \mathbf{F}_r + \mathbf{F}_h \qquad (1)$$

where $\mathbf{x}$ is a $n \times 1$ vector of task space coordinates specifying the position and orientation of the hand (for Pneu-WREX $n = 4$ and $\mathbf{x} = \begin{bmatrix} x & y & z & \theta_z \end{bmatrix}^{\mathrm{T}}$), $\mathbf{F}_r$ is an $n \times 1$ vector of

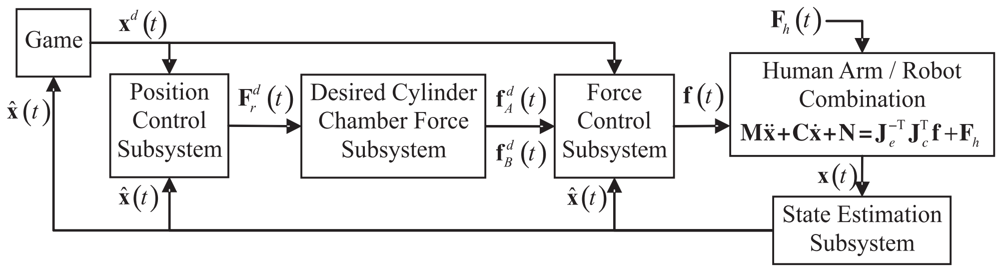

Fig. 2. Top-level controller diagram. A computer game generates desired trajectories for the controller. These trajectories are interpreted by the human subject visually on the computer screen.

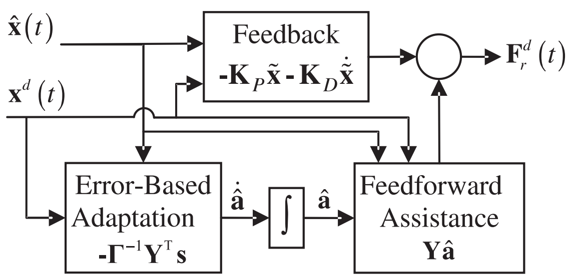

Fig. 3. Adaptive position control subsystem. The adaptive controller learns a model of the patients abilities and effort which allows the compliance of the controller to be high.

forces applied by the robot actuators which is mapped by the Jacobian to the interface location, $\mathbf{F}_h$ is an $n \times 1$ vector of forces applied by the human subject at the hand (representing human motor output), $\mathbf{M}$ is the $n \times n$ generalized inertia matrix, $\mathbf{C}$ is the $n \times n$ Coriolis matrix, and $\mathbf{N}$ is an $n \times 1$ vector of external forces acting on the robotic orthosis human arm combination, including gravitational, viscous, and spring forces. The forces, $\mathbf{F}_r$, are applied at the location of the subject's hand using the Jacobian transformation developed by Sanchez et al. (2005). The subject is secured to the robot with a hand grip and forearm cuff.

2.2. Adaptive Position Controller for Movement Training

The adaptive position control subsystem, shown in Figure 3, determines a desired spatial force, which is the input to the force control subsystem. The adaptive controller design uses the sliding surface, $\mathbf{s}$, and reference trajectory, $\mathbf{w}$ (Slotine and Li 1991). Here $\mathbf{s}$ and $\mathbf{w}$ are defined as

$$\begin{aligned} \mathbf{s} &= \dot{\tilde{\mathbf{x}}} + \mathbf{\Lambda}\tilde{\mathbf{x}} = \left(\dot{\hat{\mathbf{x}}} - \dot{\mathbf{x}}_d\right) + \mathbf{\Lambda}\left(\hat{\mathbf{x}} - \mathbf{x}_d\right) \\ \mathbf{w} &= \dot{\mathbf{x}}_\mathbf{d} - \mathbf{\Lambda}\tilde{\mathbf{x}} = \dot{\mathbf{x}}_\mathbf{d} - \mathbf{\Lambda}\left(\hat{\mathbf{x}} - \mathbf{x}_d\right) \end{aligned} \tag{2}$$

where $\tilde{\mathbf{x}}$ is the trajectory tracking error, $\hat{\mathbf{x}}$ and $\mathbf{x}_d$ are $n \times 1$ vectors of the estimated and desired location of the hand, respectively, and $\mathbf{\Lambda}$ is an $n \times n$ symmetric, constant, positive-definite, gain matrix. The control law for this method specifies the desired spatial robot force, $\mathbf{F}_r^d$, as

$$\mathbf{F}_r^d = \mathbf{Y}\left(\mathbf{x}, \dot{\mathbf{x}}, \mathbf{w}, \dot{\mathbf{w}}\right)\hat{\mathbf{a}} - \mathbf{K}_P\tilde{\mathbf{x}} - \mathbf{K}_D\dot{\tilde{\mathbf{x}}} \tag{3}$$

where $\mathbf{K}_P$ and $\mathbf{K}_D$ are symmetric, constant, positive-definite gain matrices and $\mathbf{Y}\hat{\mathbf{a}}$ is a model of the system dynamics including the forces generated by the human subject and is defined as

$$\mathbf{Y}\hat{\mathbf{a}} = \widehat{\mathbf{M}}\dot{\mathbf{w}} + \widehat{\mathbf{C}}\mathbf{w} + \widehat{\mathbf{N}} - \mathbf{F}_h \tag{4}$$

where $\widehat{\mathbf{M}}$, $\widehat{\mathbf{C}}$, and $\widehat{\mathbf{N}}$ are estimates of the dynamics of the robotic orthosis and human arm combination, $\mathbf{Y}$ is a $m \times n$ matrix of known functions of $\hat{\mathbf{x}}$, $\dot{\mathbf{x}}$, $\mathbf{w}$, and $\dot{\mathbf{w}}$, and $\hat{\mathbf{a}}$ is an $m \times 1$ vector of parameter estimates.

In order for Pneu-WREX to interact compliantly with each subject, the feedback gains $\mathbf{K}_P$ and $\mathbf{K}_D$ are kept small. In practice, the effective stiffness of the robot was 109 N m^{-1} (Wolbrecht et al. 2008). To gain an approximate feel for how compliant this made the robot, consider a scenario in which the person relaxes the arm (approximately 40 N) and the robot lifts the arm to a target. If the person now applies a sudden force equal to the weight of his arm, the robot will displace by approximately 37 cm.

The dynamic model, $\mathbf{Y}\hat{\mathbf{a}}$, should have sufficient resolution and complexity to appropriately adapt to the diverse impairment characteristics typically seen in people who have suffered a stroke or other neurological injury. The dynamic model used for Pneu-WREX uses radial basis functions to model patient output force capability as defined in Appendix A and Wolbrecht et al. (2008).

The basis function parameter estimates, $\hat{\mathbf{a}}$, are updated according to

$$\dot{\hat{\mathbf{a}}} = -\mathbf{\Gamma}^{-1}\mathbf{Y}^{\mathrm{T}}\mathbf{s} \tag{5}$$

which is required for stability from the Lyapunov analysis provided in Appendix C. We note that the stability analysis includes the compressible flow and non-linearities of the pneumatic cylinders.

In the force control law given in (3), $\mathbf{Y}\hat{\mathbf{a}}$ is an estimate of the forces required by the robotic orthosis to move the human extremity along the desired reference trajectory, $\mathbf{w}$. This model

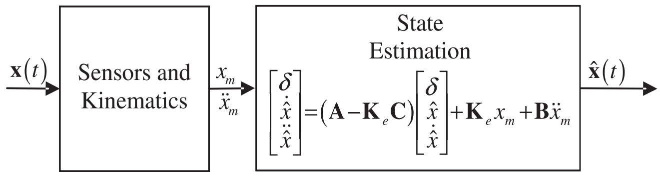

Fig. 4. State estimation subsystem. State estimation is used to obtain smooth position, velocity, and acceleration signals.

varies depending on the dynamics of the patient's extremity, the patient's neurological ability, and the patient's effort. Here $\mathbf{Y}\widehat{\mathbf{a}}$ is a feedforward term in the control law, allowing the controller to move a patient's extremity along a desired trajectory while keeping the proportional, $\mathbf{K}_P$, and derivative gains, $\mathbf{K}_D$, small, so that the resulting controlled environment feels compliant to the patient.

2.3. State Estimation

In order to improve the position and velocity signals used for the control of Pneu-WREX, two two-axis microelectromechanical system (MEMS) accelerometers (Analog Devices ADXL320EB) were installed on the end-effector of the orthosis. Using the accelerometer measurements and the forward kinematics of the position sensors, a Kalman filter was designed to estimate the position and velocity of the end-effector in task space, as shown in Figure 4. Using the forward kinematics defined in Appendix B and the spatial Jacobians developed by Sanchez et al. (2005), the end-effector velocities are mapped back to both joint and cylinder velocities.

With the accelerometers properly oriented the task space accelerations of the end-effector, $\ddot{\mathbf{x}} = \begin{bmatrix} \ddot{x} & \ddot{y} & \ddot{z} & \ddot{\theta}_z \end{bmatrix}$, can be measured. Combined with the forward kinematics, the state space equations for the measurement system are (shown below for the x direction)

$$\begin{bmatrix} \dot{\delta} \\ \dot{x} \\ \ddot{x} \end{bmatrix} = \begin{bmatrix} 0 & 0 & 0 \\ 0 & 0 & 1 \\ -\alpha & 0 & 0 \end{bmatrix} \begin{bmatrix} \delta \\ x \\ \dot{x} \end{bmatrix} + \begin{bmatrix} 0 \\ 0 \\ \alpha \end{bmatrix} \ddot{x}_m + \begin{bmatrix} 1 & 0 \\ 0 & 0 \\ 0 & -\alpha \end{bmatrix} \begin{bmatrix} v_b \\ v_a \end{bmatrix}$$

$$x_m = \begin{bmatrix} 0 & 1 & 0 \end{bmatrix} \begin{bmatrix} \delta \\ x \\ \dot{x} \end{bmatrix} + v_e \tag{6}$$

where δ and α are the accelerometer offset and scaling constants, $\ddot{x}_m$ is the voltage measurement from the accelerometer, x_m is the position measurement calculated from the forward kinematics of the joint angles as measured by the potentiometers, and v_b, v_a, and v_e are assumed to be Gaussian white measurement noise. The system in (6) has the form

$$\begin{aligned} \dot{\mathbf{r}} &= \mathbf{A}\mathbf{r} + \mathbf{B}a_m + \mathbf{B}_v v_a \\ x_m &= \mathbf{C}\mathbf{r} + v_e \end{aligned} \tag{7}$$

where $\mathbf{r} = \begin{bmatrix} \delta & x & \dot{x} \end{bmatrix}^{\mathrm{T}}$, and $\mathbf{A}$, $\mathbf{B}$, $\mathbf{B}_v$, and $\mathbf{C}$ are defined from (6). A state estimator for this system is defined as

$$\dot{\widehat{\mathbf{r}}} = \mathbf{A}\widehat{\mathbf{r}} + \mathbf{K}\left(x_m - \mathbf{C}\widehat{\mathbf{r}}\right) + \mathbf{B}a_m \tag{8}$$

where $\mathbf{K}$ is the estimator gain matrix and $\widehat{\mathbf{r}}$ is the state estimation. The error of the state estimator is

$$\mathbf{e} = \mathbf{r} - \widehat{\mathbf{r}}. \tag{9}$$

Substituting (7) and (8) into (9) gives (in the absence of noise),

$$\dot{\mathbf{e}} = (\mathbf{A} - \mathbf{K}\mathbf{C})\,\mathbf{e}. \tag{10}$$

We see from (10) that if $\mathbf{K}$ is selected so that the eigenvalues of $\mathbf{A} - \mathbf{K}\mathbf{C}$ have negative real parts, then $\mathbf{e}(t) \to 0$ as $t \to \infty$. The estimator gain matrix $\mathbf{K}_e$ was determined by solving the linear quadratic regulator problem for the system $\dot{\mathbf{q}} = \mathbf{A}'\dot{\mathbf{q}} + \mathbf{B}'\mathbf{u}'$, where $\mathbf{A}' = \mathbf{A}^{\mathrm{T}}$ and $\mathbf{B}' = \mathbf{C}^{\mathrm{T}}$. The values for the state weighting matrix $\mathbf{Q}$ and the control matrix $\mathbf{R}$ were tuned experimentally to balance the state estimation response time to its susceptibility to noise. MATLAB's *lqr* command was used to find the estimator gain matrix $\mathbf{K}_e$ for each tuning iteration. Good performance was found using the estimator gain matrix $\mathbf{K}_e = \begin{bmatrix} -316 & 101 & 5050 \end{bmatrix}^{\mathrm{T}}$. A similar estimator is used for the other task space coordinates ($\ddot{y}$, $\ddot{z}$, and $\ddot{\theta}_z$).

3. Pneumatic Force Controller

The pneumatic force controller takes the desired task-space force from (3) and determines the flow rates required from the servovalves to produce this force. These flow rates are then converted into a spool voltage using a flow map that was determined using experimental data. The following sections first describe the equations for the output force from a pneumatic cylinder and how to choose smooth individual chamber forces (Section 3.1). Next, the details of the cylinder chamber force dynamics are given in Section 3.2. In Section 3.3, the force controller with adaptive leakage compensation is presented. Section 3.4 describes the servovalve characterization.

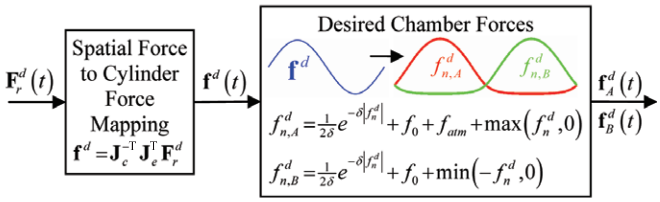

Fig. 5. Desired individual chamber force selection subsystem. Individual chamber forces are selected to produce a desired net output force. A smoothing term keeps the desired individual chamber forces smooth in their first derivatives as the desired net output force crosses zero.

3.1. Cylinder Chamber Forces

In order to define the flow control laws for the servovalves, we first need to determine the desired forces at the cylinder level, as shown in Figure 5. Starting with the forward kinematic home positions given in Appendix B, the spatial Jacobian transformations for end-effector forces, $\mathbf{J}_e$, and the cylinder forces, $\mathbf{J}_c$, developed by Sanchez et al. (2005) are used to define the relationship between the desired task forces from the controller at the human/orthosis interface, $\mathbf{F}_r^d$, and the desired cylinder forces, $\mathbf{f}^d$, according to

$$\mathbf{f}^d = \mathbf{J}_c^{-\mathrm{T}} \mathbf{J}_e^{\mathrm{T}} \mathbf{F}_{r.}^d \tag{11}$$

The desired cylinder forces, $\mathbf{f}^d$, are used to determine the desired individual chamber forces, $\mathbf{f}_A^d$ and $\mathbf{f}_B^d$. To select the individual chamber forces, we define the net output force from the nth double acting pneumatic cylinder as

$$f_n = f_{n,A} - f_{n,B} - f_{atm} \tag{12}$$

where f_n is the net output force, $f_{n,A}$ is the force on piston from the non-rod side cylinder chamber, $f_{n,B}$ is the force on piston from the rod side cylinder chamber, and f_{atm} is the force on the piston from atmospheric pressure on the exposed rod.

Pneu-WREX uses a servovalve for each cylinder chamber, allowing both $f_{n,A}$ and $f_{n,B}$ to be controlled independently. This configuration, although more expensive in terms of additional valves and electronics, is important in that it allows individual chamber pressures to be kept low, which reduces the actuation stiffness and the effects of seal friction. This allows the robot to be highly compliant and backdrivable, which are both desirable for robots for rehabilitation.

To keep the desired chamber forces continuous in their first derivatives the desired chamber forces, $f_{n,A}^d$ and $f_{n,B}^d$, are set such that the desired net output force is $f_n^d = f_{n,A}^d - f_{n,B}^d - f_{atm}$, and that

$$\begin{aligned} f_{n,A}^d &= \frac{1}{2\delta} e^{-\delta\left|f_n^d\right|} + f_0 + f_{atm} + \max\left(f_n^d, 0\right) \\ f_{n,B}^d &= \frac{1}{2\delta} e^{-\delta\left|f_n^d\right|} + f_0 + \min\left(-f_n^d, 0\right) \end{aligned} \tag{13}$$

where f_0 is the minimum chamber force, and δ is a smoothing constant. The minimum chamber force is chosen to be slightly greater than the force of atmospheric pressure on the piston head, which is the lowest possible force produced by the air in the cylinder chamber. The exponential term in (13) smoothes the desired chamber forces as the desired net output force crosses zero. This keeps $f_{n,A}$ and $f_{n,B}$ continuous in their first derivatives, which is necessary for the stability analysis. We note that most other pneumatic control researchers completely ignore this discontinuity and, as our experimental results show, doing so causes a noticeable force error or disturbance to act on the system.

As the ideal rehabilitation system is completely backdrivable, it is undesirable to have these force errors when the overall output force levels are low. Selecting δ represents a tradeoff; a smaller δ makes the exponential term in $f_{n,A}^d$ and $f_{n,B}^d$ decay slowly, but increases the average cylinder chamber force when the desired net output force is zero. Setting the desired cylinder chamber forces according to (13) keeps the average cylinder chamber pressure low if f_0 is low, thereby reducing energy consumption (Al-Dakkan et al. 2003; Granosik and Borenstein 2004) and seal friction, which improves backdrivability in zero force control mode.

3.2. Cylinder Chamber Force Dynamics

The dynamics of the force produced by air in a cylinder chamber are well documented in the literature (Bobrow and McDonell 1998; Richer and Hurmuzlu 2000a,b; Xiang and Wikander 2004). The dynamics of force for the non-rod side chambers of n cylinders can be approximated by

$$\dot{\mathbf{f}}_A = \mathbf{V}_A^{-1} k \left(RT\mathbf{A}_A \left(\dot{\mathbf{m}}_A + \mathbf{l}_A \right) - \dot{\mathbf{V}}_A \mathbf{f}_A \right) \tag{14}$$

where $\mathbf{f}_A$ is a $n \times 1$ vector of non-rod side cylinder chamber forces, k is the ratio of specific heats of air, R is the universal gas constant, T is the air temperature, $\dot{\mathbf{m}}_A$ is a $n \times 1$ vector of mass flow rates into the non-rod side cylinder chamber due to spool valve position, $\mathbf{l}_A$ is a $n \times 1$ vector of mass flow rates into the non-rod side cylinder chamber due to leakage, and $\mathbf{A}_A$ and $\mathbf{V}_A$ are $n \times n$ diagonal matrices defined as

$$\mathbf{A}_A = \begin{bmatrix} a_{A,1} & & & 0 \\ & a_{A,2} & & \\ & & \ddots & \\ 0 & & & a_{A,n} \end{bmatrix},$$

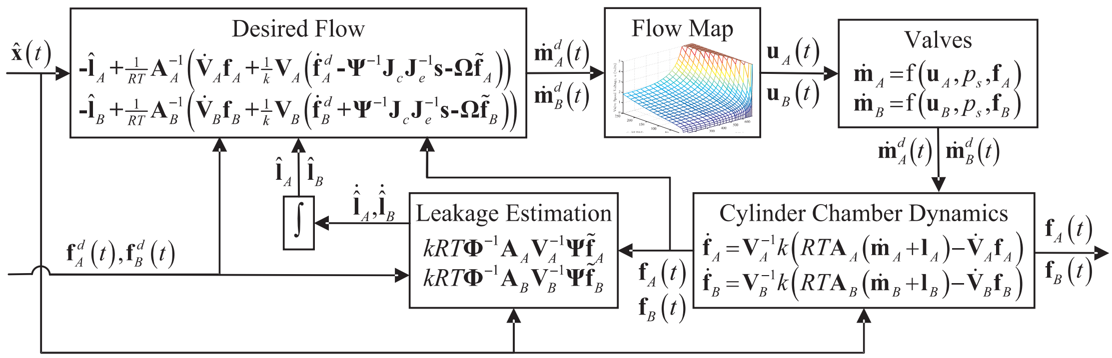

Fig. 6. Force control subsystem. The force controller determines the required spool valve voltages necessary to achieve a desired cylinder output force. The force controller includes adaptive leakage compensation. The actual chamber forces are calculated from the measured chamber pressures.

$$\mathbf{V}_A = \begin{bmatrix} v_{A,1} & & & 0 \\ & v_{A,2} & & \\ & & \ddots & \\ 0 & & & v_{A,n} \end{bmatrix}, \tag{15}$$

where $a_{A,1-n}$ and $v_{A,1-n}$ are the non-rod side piston areas and chamber volumes, respectively. The differential equation of the rod side cylinder chamber forces, $\mathbf{f}_B$, can be similarly written as

$$\dot{\mathbf{f}}_B = \mathbf{V}_B^{-1} k \left(RT\mathbf{A}_B \left(\dot{\mathbf{m}}_B + \mathbf{l}_B \right) - \dot{\mathbf{V}}_B \mathbf{f}_B \right). \tag{16}$$

3.3. Force Controller with Adaptive Leakage Compensation

The force control subsystem determines the necessary servovalve voltages required to produce the desired individual chamber forces, as shown in Figure 6. The mass flow control laws found from the Lyapunov analysis in Appendix C are

$$\begin{aligned} \dot{\mathbf{m}}_A &= -\widehat{\mathbf{l}}_A + \frac{1}{RT}\mathbf{A}_A^{-1} \\ &\times \left(\dot{\mathbf{V}}_A \mathbf{f}_A + \frac{1}{k}\mathbf{V}_A \left(\dot{\mathbf{f}}_A^d - \boldsymbol{\Psi}^{-1}\mathbf{J}_c\mathbf{J}_e^{-1}\mathbf{s} - \boldsymbol{\Omega}\widetilde{\mathbf{f}}_A \right) \right) \\ \dot{\mathbf{m}}_B &= -\widehat{\mathbf{l}}_B + \frac{1}{RT}\mathbf{A}_B^{-1} \\ &\times \left(\dot{\mathbf{V}}_B \mathbf{f}_B + \frac{1}{k}\mathbf{V}_B \left(\dot{\mathbf{f}}_B^d + \boldsymbol{\Psi}^{-1}\mathbf{J}_c\mathbf{J}_e^{-1}\mathbf{s} - \boldsymbol{\Omega}\widetilde{\mathbf{f}}_B \right) \right) \end{aligned} \tag{17}$$

where $\widehat{\mathbf{l}}_A$ and $\widehat{\mathbf{l}}_B$ are estimates of $\mathbf{l}_A$ and $\mathbf{l}_B$, respectively, and $\boldsymbol{\Psi}$ and $\boldsymbol{\Omega}$ are symmetric, constant, positive-definite gain matrices. The leakage estimates, $\widehat{\mathbf{l}}_A$ and $\widehat{\mathbf{l}}_B$, are updated according to

$$\begin{aligned} \dot{\widehat{\mathbf{l}}}_A &= kRT\boldsymbol{\Phi}^{-1}\mathbf{A}_A\mathbf{V}_A^{-1}\boldsymbol{\Omega}\widetilde{\mathbf{f}}_A \\ \dot{\widehat{\mathbf{l}}}_B &= kRT\boldsymbol{\Phi}^{-1}\mathbf{A}_B\mathbf{V}_B^{-1}\boldsymbol{\Omega}\widetilde{\mathbf{f}}_B \end{aligned} \tag{18}$$

where $\boldsymbol{\Phi}$ is symmetric, constant, positive definite gain matrix, and $\widetilde{\mathbf{f}}_A$ and $\widetilde{\mathbf{f}}_B$ are defined as

$$\begin{aligned} \widetilde{\mathbf{f}}_A &= \mathbf{f}_A - \mathbf{f}_A^d \\ \widetilde{\mathbf{f}}_B &= \mathbf{f}_B - \mathbf{f}_B^d \end{aligned} \tag{19}$$

where $\mathbf{f}_A$ and $\mathbf{f}_B$ are the actual chamber forces (as calculated from the measured chamber pressures) for the non-rod and rod side chambers of a double acting cylinder, respectively, and $\mathbf{f}_A^d$ and $\mathbf{f}_B^d$ are the corresponding desired forces (as defined previously). The novel leakage estimator (18) compensates for the leakage variance from valve to valve and increases in leakage as the valves wear-in, driving the steady-state average force error to zero.

When mass flow is proportional to spool valve position, the mass flow control laws and the leakage estimate update law (18) combine with the position adaptive control law (4) and parameter update law (5) to produce a globally asymptotically stable system for position and force control. However, in most cases one cannot directly control the mass flow through a servovalve, since the flow is a highly non-linear function of supply pressure, chamber pressure, and spool position. In other words, the control voltage sent to the servovalve defines the spool position but not the mass flow rate needed in the control law (17). We address this problem by creating a flow map of the servovalve from experimental data, which is explained in the next section.

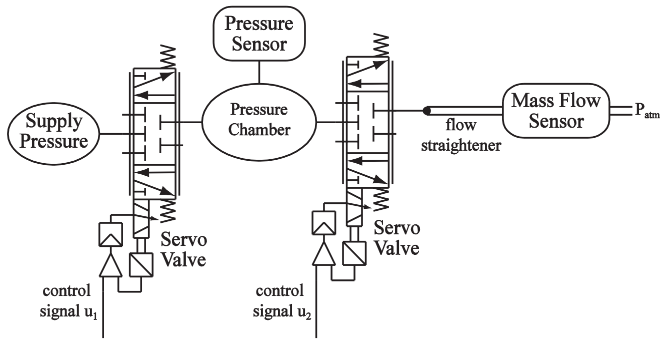

Fig. 7. Experimental setup for flow measurements.

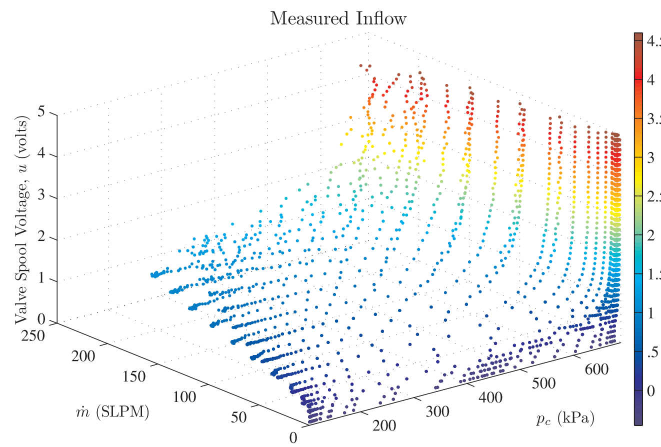

Fig. 8. Measured mass air flow into the chamber. To simplify the equation fitting, the valve offset voltage (5 volts) was subtracted from the measured data.

3.4. Servovalve Characterization

The mass flow rate, $\dot{m}$, through a servovalve is in general a function of valve spool position u, supply pressure p_s, and the chamber pressure, p_c. Past work has modeled the mass flow of air through a servovalve as mass flow through a variable orifice (Sanville 1971) or a nozzle. This approach has been combined with dead band compensation (Xiang and Wikander 2004). Others have added detailed effective flow area calculations (Richer and Hurmuzlu 2000a,b). These methods typically define separate equations for choked and unchoked flow, based on a critical pressure. These theoretical flow equations have been shown to be only approximations of actual mass flow through a servovalve (Bobrow and McDonell 1998). In addition, it is difficult, at best, to combine theoretical flow equations with the variable orifice effects of the spool valve dead band. For these reasons, the control of Pneu-WREX, the mass flow relationship for the Festo servovalve (model MPYE-5-1/8-LF-010-B), was determined experimentally.

Flow experiments have been performed in the past by Bobrow and McDonell (1998) and Granosik and Borenstein (2004) and others. For our experiments, two servovalves were set up in series with a chamber in the middle (see Figure 7).

Air was supplied to the first servovalve at 690 kPa and exhaust flow was measured on the second servovalve using a Honeywell AWM720P1 mass air flow sensor. This configuration is necessary because the mass flow sensor has a maximum pressure rating significantly lower than the supply pressure. The control voltage, u, for each valve was varied independently, creating different chamber pressure and flow combinations. This process was automated, which greatly reduced data collection time. Chamber pressure, p_c, and mass air flow, $\dot{m}$, were measured for each steady-state flow condition. Owing to conservation of mass, the mass air flow data collected characterizes both flow into a chamber (through the first valve) and flow out of a chamber (through the second valve). Figure 8 shows data collected from the first servovalve, representing flow into the chamber from one of the experiments. To simplify the equation fitting, the valve offset voltage (5 V) was subtracted from the measured data (the Festo valve operates from 0 to 10 V with zero flow at 5 V).

Attempts to fit the inflow data to the previously mentioned analytical functions resulted in a poor fit. Different functions were experimented with in order to find surfaces that better approximated the data. The best fitting function we found for inflow is

$$u = c_1 \frac{\dot{m}^2}{\left(1 - p_c^{2.8}\right)^{q_1}} + c_2 \frac{\dot{m}^{1/5}}{\left(1 - p_c^{2.8}\right)^{q_2}} + c_3 \dot{m}^{1/5} \tag{20}$$

where u is the servovalve spool voltage, $\dot{m}$ is the required mass flow, p_c is the chamber pressure, and c_{1-3} and q_{1-2} are the fitting constants.

To determine the constants in (20)

$$J = \|\mathbf{A}(q)\,\mathbf{C} - \mathbf{B}\|^2 \tag{21}$$

was used as the cost function, where $\mathbf{C} = [c_1 \quad c_2 \quad c_3]^{\mathrm{T}}$ and $\mathbf{A}(q)$ and $\mathbf{B}$ have rows corresponding to each measured data point, with each row defined as

$$\begin{aligned} \mathbf{A}_i &= \left[\ \dot{m}_i^2 / \left(1 - p_{c,i}^{2.8}\right)^{q_1} \quad \dot{m}_i^{1/5} / \left(1 - p_{c,i}^{2.8}\right)^{q_2} \quad \dot{m}_i^{1/5}\ \right], \\ \mathbf{B}_i &= [u_i]. \end{aligned} \tag{22}$$

The cost function was minimized in an iterative two-step process. For the first step the q were held constant and the backslash operator in Matlab was used to perform multiple linear regression to find the c. In the second step the Matlab function *fminunc* was used for a non-linear minimization of the q while holding the c at the values determined from the previous step. These two steps were repeated until the q and the c converged. The converged values for the Festo valve are

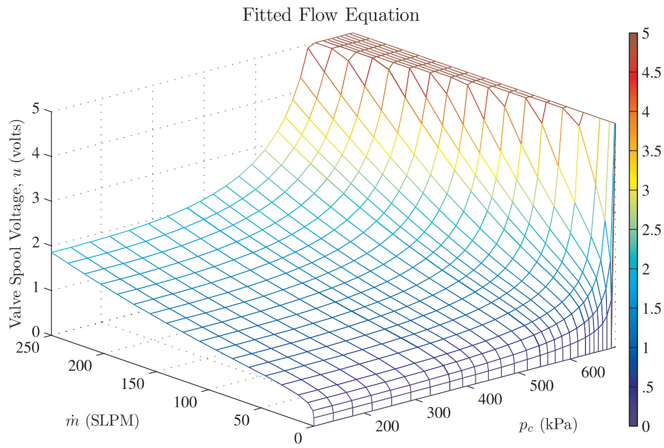

Fig. 9. Inflow surface showing required servovalve spool voltage as a function of desired mass flow rate and chamber pressure. The map is truncated at 5 V (the maximum of the valve).

$$q_{1-2} = \begin{bmatrix} 1.30 & 0.530 \end{bmatrix},$$
$$c_{1-3} = \begin{bmatrix} 1.41 & 0.351 & -0.0319 \end{bmatrix}. \tag{23}$$

These constants with (20) describe a surface relating the required servovalve spool voltage, u, to achieve a required mass flow rate, $\dot{m}$, based on current chamber pressure, p_c. This surface is illustrated in Figure 9.

As the outflow data was significantly different than the inflow data, a different function was necessary to achieve a good fit of the outflow. To simplify the equation fitting, the valve offset voltage (5 V) was subtracted from the measured data, and the resulting values were negated (thus making the measured outflow spool voltages range from 0 to 5 V like the inflow data). The equation for outflow is

$$\begin{aligned} u &= d_1 \frac{\dot{m}}{\left(1 - p_c^{1.4}\right)^{r_1}} + d_2 \frac{\dot{m}^2}{\left(1 - p_c^{1.4}\right)^{r_2}} + d_3 \frac{\dot{m}^2}{\left(1 - p_c^{2.8}\right)^{r_3}} \\ &+ d_4 \frac{\dot{m}}{\left(1 - p_c^{2.8}\right)^{r_4}} + d_5 \dot{m} + d_6 \dot{m}^{1/2} + d_7 \dot{m}^{1/4}. \end{aligned} \tag{24}$$

Using the same method previously described, the r and the d were determined to be

$$r_{1-4} = \begin{bmatrix} 0.757 & 1.50 & 0.233 & 0.963 \end{bmatrix},$$
$$d_{1-7} = \begin{bmatrix} 0.0109 & 6.77 \times 10^{-6} & 3.02 \times 10^{-5} \\ -0.00737 & -0.0135 & -0.109 & 0.157 \end{bmatrix}. \tag{25}$$

Equation (24) with the constants in (25) is used to determine the necessary servovalve spool voltage to achieve a required mass flow rate at a given chamber pressure. The force controller in Pneu-WREX uses both the inflow and outflow fitted equations to determine the necessary spool voltages to achieve the mass flow rates required from the mass flow control law of (17).

4. Testing and Results

The previously described controller includes state estimation, force control, and position control subsystems. The force controller depends on the state estimator, and position controller depends on both the force controller and the state estimator. All three of these subsystems were tested as described in the previous sections.

4.1. State Estimation Testing

Two tests were completed to evaluate the Kalman state estimator. In both tests, the state estimator is compared with signals conditioned with 50 Hz low-pass Butterworth filters (a common filter choice for control applications). In the first test, the end-effector of the orthosis was oscillated in the x direction. During this test three sets of position and velocity signals in the x direction were recorded: unfiltered signals (using a discrete derivative for velocity), 50 Hz low-pass filtered signals, and Kalman state estimates. The controller remained off for the entire test. The goal of this first test was to compare the Kalman state estimator to the type of motions typically used for our robotics applications. Important measures for comparison include both phase lag and noise, both of which are detrimental to controller stability. Figure 10 shows position and velocity from the 50 Hz low-pass filters, the Kalman state estimator, and the unfiltered signals.

The results show that the Kalman filtered signals have less noise and less phase lag than the low-pass filtered signals. Decreasing the low-pass filter frequency would decrease the signal noise, but would introduce more phase lag, and therefore degrade the stability of the system. In the second experiment we tracked a 5 cm peak-to-peak position sine wave with a 1 Hz frequency in the x direction of task space. This experiment was repeated twice, with the controller using the Kalman state estimator signals the first time and the controller using 50 Hz low-pass filtered signals the second time. The goal of this experiment was to see how the use of the Kalman state estimator affects the response of the closed-loop system. The control voltage sent to a single cylinder chamber during this test is shown in Figure 11. The results in Figure 11 demonstrate how the use of the Kalman state estimator significantly reduces controller effort. This reduced controller effort consumes less energy and produces less audible noise.

The results shown in Figures 10 and 11 are significant to the stability of the robot, in that there is a marked reduction

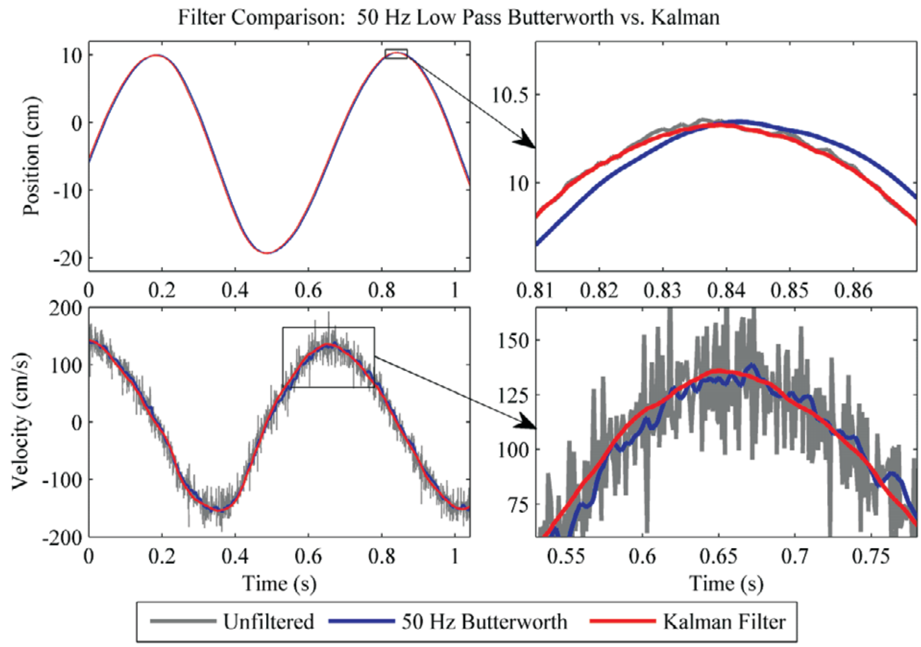

Fig. 10. Filtering comparison for position and velocity signals. The end-effector was oscillated in the x direction. The top left plot shows the position of the end-effector, with a magnified view of this plot shown in the top right plot (as indicated by the box and arrow). The bottom left plot shows the velocity of the end-effector in the x direction, with a magnified view of this plot shown in the bottom right plot (as indicated by the box and arrow). Unfiltered, low-pass filtered (50 Hz Butterworth), and Kalman filtered signals are shown in all four plots. Note how the Kalman filtered signals have less noise and less phase lag than the low-pass filtered signals.

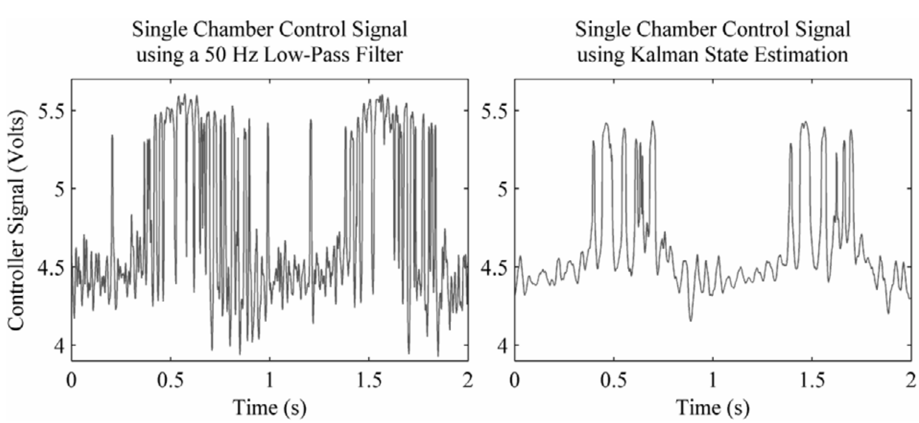

Fig. 11. Controller effort using Kalman state estimation versus using 50 Hz low-pass filtered signals. The controller using the Kalman state estimator (right-hand side plot) is significantly smoother, producing less audible noise and consuming less pneumatic and electrical energy.

is signal noise and phase lag, which reduces the controllable bandwidth of the system, as well as a reduction in controller effort and control signal frequency, which can excite the natural mechanical and pneumatic frequency of the robot, further reducing system stability.

4.2. Force Controller Testing

Two tests were performed to evaluate force controller performance. In the first test we compared the force controller with and without the smoothing term in (13). For the experiments without the smoothing term, we simply omitted the exponen-

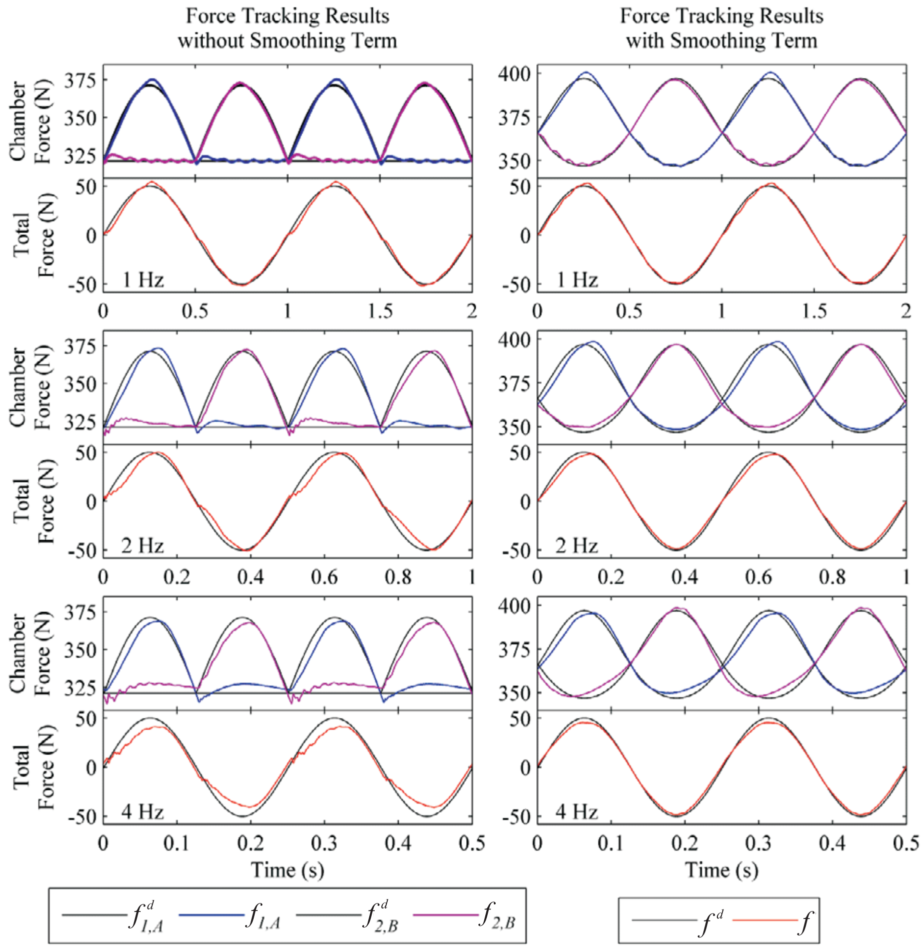

Fig. 12. Force tracking results with (right column) and without (left column) the inclusion of a smoothing term. The desired and actual total forces are shown on the bottom half of each row and the desired and actual chamber forces are shown in the top half of each row. The desired total force is a peak-to-peak 50 N sine wave at 1 Hz (top row), 2 Hz (middle row), and 4 Hz (bottom row).

tial term so that the desired non-rod side chamber force, $f^d_{n,A}$, and the rod side chamber force, $f^d_{n,B}$ are set according to

$$f^d_{n,A} = f_0 + f_{atm} + \max\left(f^d_n, 0\right)$$

$$f^d_{n,B} = f_0 + \min\left(-f^d_n, 0\right) \tag{26}$$

for a given desired total cylinder force, f^d_n. As low friction cylinders are used, and individual chamber pressures are kept low, the forces from seal friction are small and have been assumed to be zero. For both experiments (with and without a smoothing term), the desired total force was a 50 N peak-to-peak sine wave. The cylinder used in these experiments had a 5.08 cm bore and 7.62 cm stroke. For this experiment, the rod end of the cylinder was held in a fixed position. At different piston positions the nonlinear controller accounts for the change in chamber air volume. However, the change in volume changes the length of the air column in the controlled chamber, and thus will moderately affect the force controller performance. The volumes of the non-rod side and rod side chambers during these experiments were 157 and 182 cm^3, respectively. The results for 1, 2, and 4 Hz tracking are shown in Figure 12.

The results shown in Figure 12 demonstrate how the smoothing term in (13) improves force control by keeping the transition from positive to negative desired force (and vice versa) continuous in the first derivative.

In the second test of the force controller we evaluated the frequency response by tracking a 50 N peak-to-peak sine wave in a single cylinder at multiple frequencies. As in the previous force tracking experiment, the cylinder had a 5.08 cm bore and 7.62 cm stroke. In addition, the rod of the cylinder was held fixed, with the non-rod side and rod side chambers having 157 and 182 cm^3 volumes, respectively. Force tracking results at 1, 2, 4, 10, 20, and 40 Hz are shown in Figure 13. The results

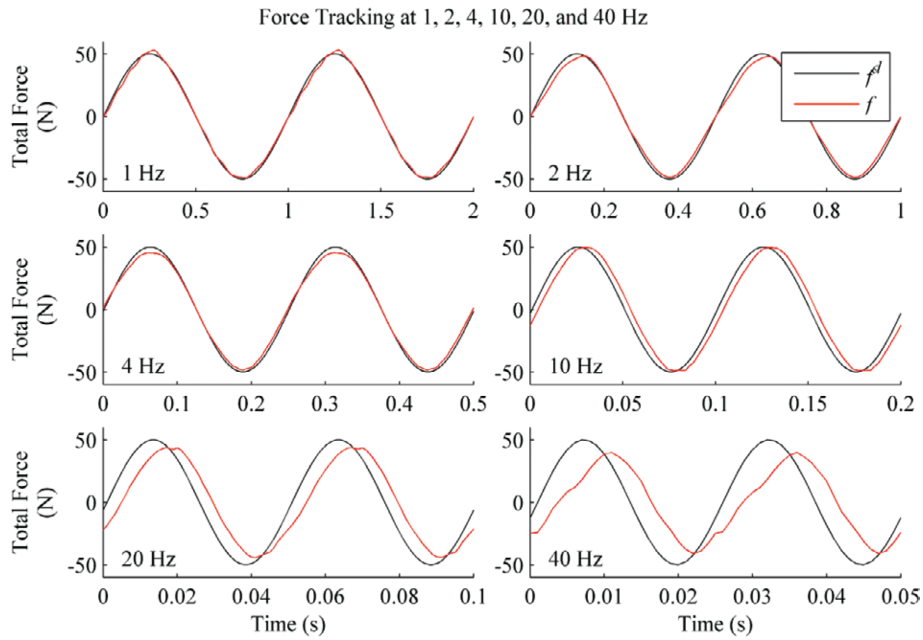

Fig. 13. Force tracking for a single cylinder at multiple frequencies. The desired force is a 50 N peak-to-peak sine wave. Results for 1, 2, 4, 10, 20, and 40 Hz are shown in the top left, top right, middle left, middle right, bottom left, and bottom right plots, respectively.

show good tracking at frequencies up to 20 Hz or higher for a single cylinder chamber.

The results from both force tracking experiments, shown in both Figure 12 and Figure 13 are from one cylinder in the completed Pneu-WREX orthosis. Owing to the mechanical design and plumbing layout, the distances between the servovalves and the cylinders is significantly larger than those typically presented in the pneumatic control literature. Improved overall force tracking performance and a higher frequency response should be possible by shortening the distance between the servovalves and the pneumatic cylinders.

4.3. Position Controller Testing

Two separate tests were performed to evaluate the position tracking of the adaptive controller. In the first test, the orthosis tracked a 5 cm peak-to-peak sine wave in the x direction (left to right with respect to the orientation of a subject in the orthosis) at multiple frequencies. The goal of this test was to evaluate small amplitude tracking for multiple frequencies. The results for tracking 0.5, 1, and 2 Hz sine waves are shown in Figure 14.

The results show good tracking position tracking for up to 2 Hz after the adaptation parameters had reached a steady state. By reducing the amplitude of the sine wave, slightly higher frequencies can be maintained. Such higher frequencies, however, are not typically used for rehabilitative movement training.

In the second position tracking test, the orthosis tracked a minimum jerk trajectory in task space at a speed typical for movement training. The goal of this test was to evaluate tracking for a typical training movement, and to verify the performance both with and without a human subject's arm connect to the device. In the test a repeated minimum jerk trajectory was tracked from –20 to 20 and then back to 20 cm in the x direction of task space (left to right with respect to the orientation of the subject). The desired trajectory had a peak velocity of 14.8 cm s^{-1}, which is within the range of normal movement training. This test was repeated for both with (bottom row) and without (top row) a subject's arm in the orthosis, as shown in Figure 15. The subject relaxed his arm when it was in the orthosis.

The results from the test demonstrate the ability of the controller to achieve good tracking for both unloaded (orthosis only) and loaded (orthosis with a subject's arm attached) conditions.

5. Discussion and Conclusions

The ideal robotic device for movement training after stroke should be strong, lightweight, and compliant, making the use of traditional actuators, such as electric motors, problematic. Pneumatic actuators have a high strength-to-weight ratio and are inherently compliant, making them good candidates for robotic movement training devices.

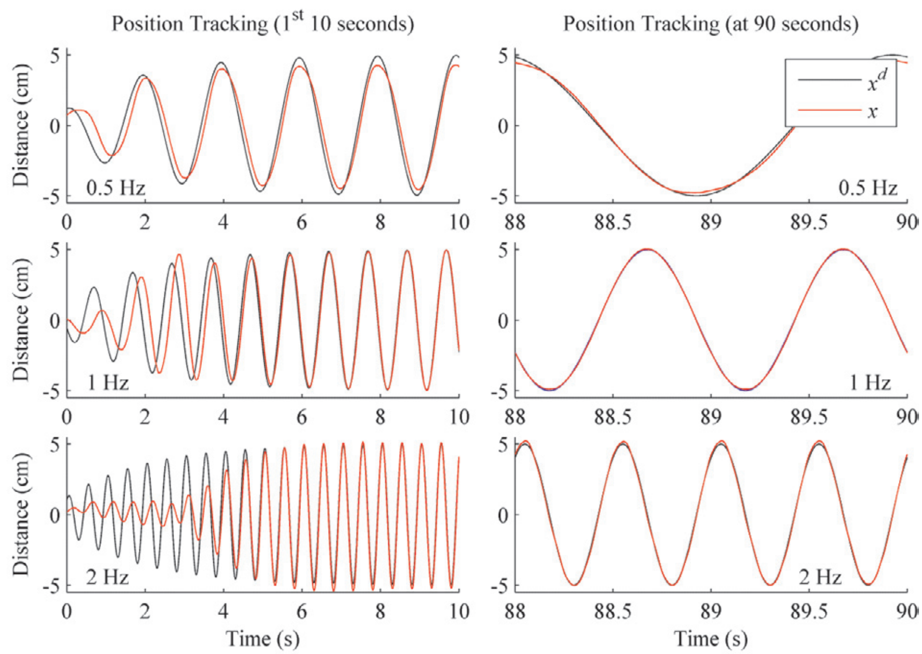

Fig. 14. Adaptive controller position tracking results. The robotic orthosis tracked a 5 cm peak-to-peak sine wave in the x direction (left to right) of task space for a period of 90 seconds. The left column shows the first 10 seconds, where the desired sine wave was gradually introduced and most of the parameter adaptation took place. The right column shows the last 2 seconds of tracking where the parameters had reached steady state. The first, second, and third rows show desired tracking frequencies of 0.5, 1, and 2 Hz, respectively.

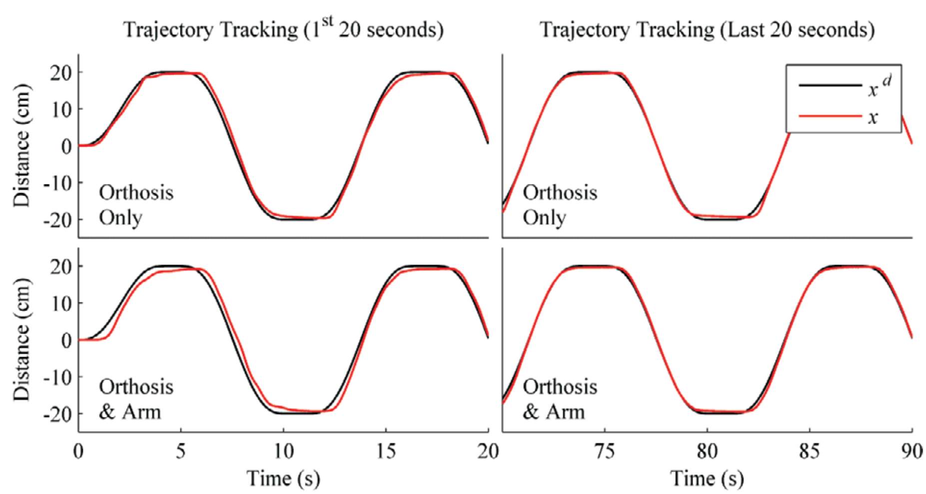

Fig. 15. Minimum jerk trajectory tracking results for a large movement. The robotic orthosis tracked a minimum jerk trajectory from left (–20) to right (20) with a peak velocity of 14.8 cm s^{-1} and a frequency of 0.1 Hz. The left column shows the first 20 seconds of tracking and the right column shows seconds 70–90. The top row results are for the orthosis only, the bottom row for the orthosis with a subject's arm connected. In both cases, the controller adaptation produces good tracking in the steady state.

In this paper we have presented an adaptive controller for a pneumatically actuated orthosis that exhibits good control for robotic movement training with human subjects. The controller includes adaptation for both the inner (force control) and outer (position control) layers of the controller. We developed several techniques to improve the performance of pneumatic systems, including the use of a Kalman filter for state estimation which decreases control effort, valve chatter, and the audible noise of the system.

The results presented in this paper show that the adaptive controller implemented for the pneumatic orthosis, named Pneu-WREX, achieves cylinder chamber force control in excess of 20 Hz and small amplitude position tracking in task space up to 2 Hz. Additional results show how the adaptive controller achieves good tracking for a typically large minimum jerk trajectory training movement both with and without a subject's arm connected to the device.

The robotic movement training device is lightweight, strong, compliant, and assists when the subject is unable to by forming a model of the patients' abilities. The resulting compliant environment gives the human subject a sense of control over the movement training.

Acknowledgement

This work was supported in part by NIH N01-HD-3-3352 and NCRR M01RR00827.

Appendix A: Impairment Modeling with Radial Basis functions

In the current implementation of Pneu-WREX (see also Wolbrecht et al. (2008)), the regressor matrix $\mathbf{Y}\widehat{\mathbf{a}}$ comprises spatially dependent Gaussian radial basis functions, defined as

$$g_n = \exp\left(-\left\|\mathbf{x} - \boldsymbol{\mu}_n\right\|^2 / 2\sigma^2\right) \tag{27}$$

where g_n is the nth radial basis function, $\mathbf{x}$ is the current location of the patient's hand, $\boldsymbol{\mu}_n$ is the location of the nth radial basis function, and σ is effectively a scalar smoothing constant that determines the width of the basis function. For Pneu-WREX we have implemented a three-dimensional grid of radial basis functions, with eight grid divisions left to right ($-x$ to $+x$), five grid divisions in and out ($-y$ to $+y$), and three grid divisions down to up ($-z$ to $+z$) across the workspace of the robot, and with $\sigma = 7.62$ cm. The grid divisions are evenly spaced at 10 cm apart. The value of σ changes the width of each radial basis function so it must be determined in conjunction with the grid spacing, so that there is sufficient overlap in the radial basis functions to achieve good function approximation. The grid spacing was chosen to be small enough to obtain reasonable spatial variance in the function approximation but without adding excessive computational expense for real-time control. The vector of all of the Gaussian radial basis functions is defined as

$$\mathbf{g} = \begin{bmatrix} g_1 & g_2 & \ldots & g_{120} \end{bmatrix}^{\mathrm{T}}. \tag{28}$$

We combine this vector of Gaussian radial basis functions to define the regressor matrix $\mathbf{Y}$ as

$$\mathbf{Y}^{3x360} = \left[\begin{array}{c|c|c} \mathbf{g}^{\mathrm{T}} & 0 & 0 \\ \hline 0 & \mathbf{g}^{\mathrm{T}} & 0 \\ \hline 0 & 0 & \mathbf{g}^{\mathrm{T}} \end{array}\right]. \tag{29}$$

The parameter estimate vector, $\widehat{\mathbf{a}}$, is therefore a 360×1 vector, with the parameters representing the amount of force the subject is unable to provide to hold their arm at a particular location in space. Including more parameters (e.g. more basis functions) is possible and would allow the model to represent more complicated impairment, but would also increase the computational expense. When all of the inertial and gravitational terms of (4) are included, and the force output from the human subject remains time independent, the controller defined by (3) and (5) is globally asymptotically stable. For the implementation with Pneu-WREX used here, however, the inertial components of the dynamic model were omitted because the movements of interest were relatively slow and doing so resulted in a significant reduction in the real-time computational load.

Appendix B: Pneu-WREX Kinematics

The forward kinematics for Pneu-WREX follow the method first developed by Sanchez et al. (2005). In addition, the serial chain is simplified, removing the need for $\mathbf{q}_{3b}$ and $\mathbf{q}_{4b}$. The revised home position coordinates necessary for the forward kinematic analysis methods of Murray et al. (1994) are (the origin of these points is at the center of the patient's impaired shoulder)

$$\left[\mathbf{q}_1, \mathbf{q}_2, \mathbf{q}_3, \mathbf{q}_4, \mathbf{q}_5, \mathbf{q}_{5b}\right] = \begin{bmatrix} 0 & -3.91 & -3.91 & -3.91 & 0.09 & -0.016 \\ 0 & 0 & 1.4 & 1.4 + ua & 2.95 + ua & 1.25 + ua \\ 0 & 0 & -v - 3 & -v - 3 & -v - 6.375 & -v - 6.375 \end{bmatrix}$$

$$\left[\mathbf{q}_{c1b}, \mathbf{q}_{c2b}, \mathbf{q}_{c3b}, \mathbf{q}_{c4b}\right] = \begin{bmatrix} -2.125 & -5.351 & -6.474 & -6.574 \\ -12.9 & -20.75 & 1.4 & -6.8 \\ 0 & 0 & -v - 1.5 & -v - 8.2 \end{bmatrix}$$

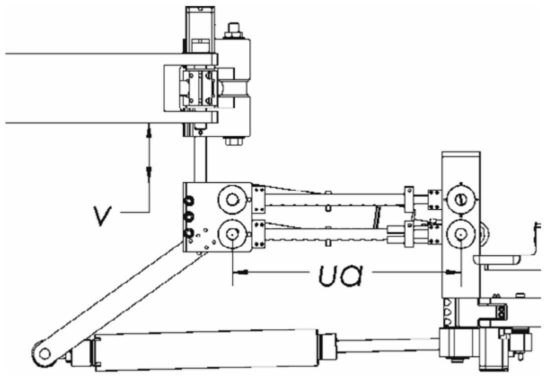

Fig. 16. Upper arm length, ua, and shoulder height, v, definitions.

$$\left[\mathbf{q}_{c1r}, \mathbf{q}_{c2r}, \mathbf{q}_{c3r}, \mathbf{q}_{c4r}\right] = \begin{bmatrix} -2.15 & -5.377 & -6.474 & -6.29 \\ 0 & 1.467 & 12.051 & 3.454 + ua \\ 0 & 0 & -v-3 & -v-7.692 \end{bmatrix}$$

$$\mathbf{q}_{arm} = \mathbf{q}_5 + \mathbf{hand} \tag{30}$$

where variables ua and v define the length of the upper arm, and the distance between the upper-shoulder joint and the shoulder in inches, respectively (see Figure 16).

In addition in (30) above, $\mathbf{q}_i$ are points on the joint axes, $\mathbf{q}_{cib}$ are points on the cylinder base axes, $\mathbf{q}_{cir}$ are points on the cylinder rod axes, $\mathbf{q}_{arm}$ is the location of the interface between Pneu-WREX and the subject's forearm, and $\mathbf{hand} = \left[arm_x \quad arm_y \quad arm_z\right]^{\mathrm{T}}$ is the location of the hand with respect to the last axis, $\mathbf{q}_5$. The locations of these points are depicted in Figure 17.

Pneu-WREX has six rotation axes. The angles about the rotation axes are defined as

$$\boldsymbol{\theta}_{full} = \begin{bmatrix} \theta_1 & \theta_2 & \theta_3 & \theta_4 & \theta_5 & \theta_{5b} \end{bmatrix}^{\mathrm{T}} \tag{31}$$

where $\boldsymbol{\theta}_{full}$ is the full 6×1 vector of all joint axes on Pneu-WREX. The axes of rotation are defined as

$$\begin{bmatrix} \omega_1 & \omega_2 & \omega_3 & \omega_4 & \omega_5 & \omega_{5b} \end{bmatrix} = \begin{bmatrix} 0 & 0 & 1 & 1 & 0 & 0 \\ 0 & 0 & 0 & 0 & 0 & 0 \\ 1 & 1 & 0 & 0 & 1 & 1 \end{bmatrix} \tag{32}$$

where ω_i are unit vectors along each axis of rotation. The location of these rotation axes are shown in Figure 17.

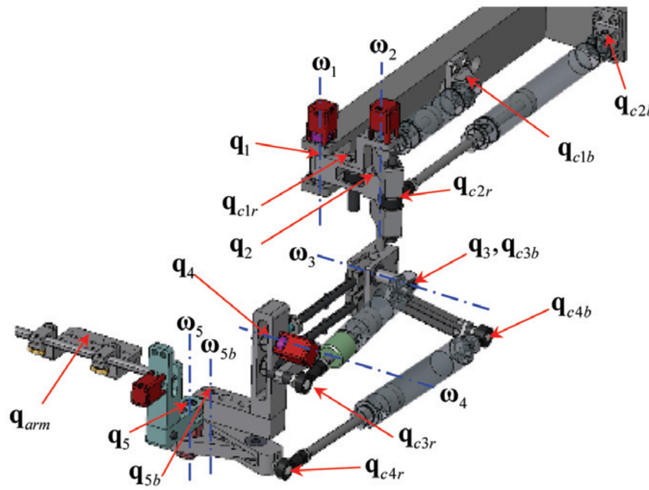

Fig. 17. Pneu-WREX home positions for kinematic equations.

Appendix C: Lyapunov Stability Analysis

For the stability analysis of the adaptive position control applied to a pneumatic system, we consider the Lyapunov function candidate:

$$\begin{aligned} V(t) &= \frac{1}{2}\mathbf{s}^{\mathrm{T}}\mathbf{M}\mathbf{s} + \frac{1}{2}\tilde{\mathbf{x}}^{\mathrm{T}}\left(\mathbf{K}_P + \boldsymbol{\Lambda}\mathbf{K}_D\right)\tilde{\mathbf{x}} + \frac{1}{2}\tilde{\mathbf{a}}^{\mathrm{T}}\boldsymbol{\Gamma}\tilde{\mathbf{a}} \\ &+ \frac{1}{2}\tilde{\mathbf{f}}_A^{\mathrm{T}}\boldsymbol{\Psi}\tilde{\mathbf{f}}_A + \frac{1}{2}\tilde{\mathbf{f}}_B^{\mathrm{T}}\boldsymbol{\Psi}\tilde{\mathbf{f}}_B + \frac{1}{2}\tilde{\mathbf{l}}_A^{\mathrm{T}}\boldsymbol{\Phi}\tilde{\mathbf{l}}_A + \frac{1}{2}\tilde{\mathbf{l}}_B^{\mathrm{T}}\boldsymbol{\Phi}\tilde{\mathbf{l}}_B \end{aligned} \tag{33}$$

where $\mathbf{s}$, $\mathbf{M}$, $\tilde{\mathbf{x}}$, $\mathbf{K}_P$, $\mathbf{K}_D$, $\boldsymbol{\Lambda}$, $\boldsymbol{\Gamma}$, $\boldsymbol{\Psi}$, $\boldsymbol{\Phi}$, $\tilde{\mathbf{f}}_A$, and $\tilde{\mathbf{f}}_B$ are as defined previously, $\tilde{\mathbf{a}}$, $\tilde{\mathbf{l}}_A$, and $\tilde{\mathbf{l}}_B$, are parameter estimate errors defined as

$$\begin{aligned} \tilde{\mathbf{a}} &= \hat{\mathbf{a}} - \mathbf{a} \\ \tilde{\mathbf{l}}_A &= \hat{\mathbf{l}}_A - \mathbf{l}_A \\ \tilde{\mathbf{l}}_B &= \hat{\mathbf{l}}_B - \mathbf{l}_B \end{aligned} \tag{34}$$

where $\hat{\mathbf{a}}$, $\hat{\mathbf{l}}_A$, and $\hat{\mathbf{l}}_B$ are parameter estimates as defined previously, and $\mathbf{a}$, $\mathbf{l}_A$, and $\mathbf{l}_B$ are the actual parameter values. Taking the derivative of (33) along system trajectories gives

$$\begin{aligned} \dot{V}(t) &= \frac{1}{2}\mathbf{s}^{\mathrm{T}}\dot{\mathbf{M}}\mathbf{s} + \mathbf{s}^{\mathrm{T}}\mathbf{M}\dot{\mathbf{s}} + \tilde{\mathbf{x}}^{\mathrm{T}}\left(\mathbf{K}_P + \boldsymbol{\Lambda}\mathbf{K}_D\right)\dot{\tilde{\mathbf{x}}} + \tilde{\mathbf{a}}^{\mathrm{T}}\boldsymbol{\Gamma}\dot{\tilde{\mathbf{a}}} \\ &+ \tilde{\mathbf{f}}_A^{\mathrm{T}}\boldsymbol{\Psi}\dot{\tilde{\mathbf{f}}}_A + \tilde{\mathbf{f}}_B^{\mathrm{T}}\boldsymbol{\Psi}\dot{\tilde{\mathbf{f}}}_B + \tilde{\mathbf{l}}_A^{\mathrm{T}}\boldsymbol{\Phi}\dot{\tilde{\mathbf{l}}}_A + \tilde{\mathbf{l}}_B^{\mathrm{T}}\boldsymbol{\Phi}\dot{\tilde{\mathbf{l}}}_B. \end{aligned} \tag{35}$$

Using the sliding surface, $\mathbf{s}$, and reference trajectories, $\mathbf{w}$, defined in (2), the system dynamics in (1) can be redefined as

$$\mathbf{M}\dot{\mathbf{s}} + \mathbf{C}\mathbf{s} + \mathbf{Y}\mathbf{a} = \mathbf{F}_r. \tag{36}$$

Next, substituting for $\mathbf{M}\dot{\mathbf{s}}$ from (36) into (35), and using the fact that $\dot{\mathbf{M}} - 2\mathbf{C}$ is skew-symmetric, gives

$$\begin{aligned}\dot{V}(t) &= \mathbf{s}^{\mathrm{T}}(\mathbf{F}_r - \mathbf{Y}\mathbf{a}) + \widetilde{\mathbf{x}}^{\mathrm{T}}(\mathbf{K}_P + \boldsymbol{\Lambda}\mathbf{K}_D)\dot{\widetilde{\mathbf{x}}} + \widetilde{\mathbf{a}}^{\mathrm{T}}\boldsymbol{\Gamma}\dot{\widetilde{\mathbf{a}}} \\ &+ \widetilde{\mathbf{f}}_A^{\mathrm{T}}\boldsymbol{\Psi}\dot{\widetilde{\mathbf{f}}}_A + \widetilde{\mathbf{f}}_B^{\mathrm{T}}\boldsymbol{\Psi}\dot{\widetilde{\mathbf{f}}}_B + \widetilde{\mathbf{l}}_A^{\mathrm{T}}\boldsymbol{\Phi}\dot{\widetilde{\mathbf{l}}}_A + \widetilde{\mathbf{l}}_B^{\mathrm{T}}\boldsymbol{\Phi}\dot{\widetilde{\mathbf{l}}}_B. \qquad (37)\end{aligned}$$

The task space robot force error, $\widetilde{\mathbf{F}}_r$, in (37) is defined as

$$\widetilde{\mathbf{F}}_r = \mathbf{F}_r - \mathbf{F}_r^d \qquad (38)$$

where $\mathbf{F}_r^d$ is the desired task space robot force and $\mathbf{F}_r$ is the actual task space robot force. Substituting for $\mathbf{F}_r$ from (38) and for $\widehat{\mathbf{a}}$ from (34) into (37) gives

$$\begin{aligned}\dot{V}(t) &= \mathbf{s}^{\mathrm{T}}\left(\mathbf{F}_r^d - \mathbf{Y}\widehat{\mathbf{a}}\right) + \widetilde{\mathbf{F}}_r^{\mathrm{T}}\mathbf{s} + \widetilde{\mathbf{x}}^{\mathrm{T}}(\mathbf{K}_P + \boldsymbol{\Lambda}\mathbf{K}_D)\dot{\widetilde{\mathbf{x}}} \\ &+ \widetilde{\mathbf{a}}^{\mathrm{T}}\left(\boldsymbol{\Gamma}\dot{\widehat{\mathbf{a}}} + \mathbf{Y}^{\mathrm{T}}\mathbf{s}\right) + \widetilde{\mathbf{f}}_A^{\mathrm{T}}\boldsymbol{\Psi}\dot{\widetilde{\mathbf{f}}}_A + \widetilde{\mathbf{f}}_B^{\mathrm{T}}\boldsymbol{\Psi}\dot{\widetilde{\mathbf{f}}}_B + \widetilde{\mathbf{l}}_A^{\mathrm{T}}\boldsymbol{\Phi}\dot{\widetilde{\mathbf{l}}}_A \\ &+ \widetilde{\mathbf{l}}_B^{\mathrm{T}}\boldsymbol{\Phi}\dot{\widetilde{\mathbf{l}}}_B. \qquad (39)\end{aligned}$$

Now use the desired force control law (4) and the parameter update law (5) in (39) to further simplify the Lyapunov function derivative:

$$\begin{aligned}\dot{V}(t) &= -\widetilde{\mathbf{x}}^{\mathrm{T}}\boldsymbol{\Lambda}\mathbf{K}_P\widetilde{\mathbf{x}} - \dot{\widetilde{\mathbf{x}}}^{\mathrm{T}}\mathbf{K}_D\dot{\widetilde{\mathbf{x}}} + \widetilde{\mathbf{F}}_r^{\mathrm{T}}\mathbf{s} + \widetilde{\mathbf{f}}_A^{\mathrm{T}}\boldsymbol{\Psi}\dot{\widetilde{\mathbf{f}}}_A \qquad (40) \\ &+ \widetilde{\mathbf{f}}_B^{\mathrm{T}}\boldsymbol{\Psi}\dot{\widetilde{\mathbf{f}}}_B + \widetilde{\mathbf{l}}_A^{\mathrm{T}}\boldsymbol{\Phi}\dot{\widetilde{\mathbf{l}}}_A + \widetilde{\mathbf{l}}_B^{\mathrm{T}}\boldsymbol{\Phi}\dot{\widetilde{\mathbf{l}}}_B.\end{aligned}$$

To continue the derivation, we introduce the spatial Jacobian transformations for end-effector forces, $\mathbf{J}_e$, and the cylinder forces, $\mathbf{J}_c$, developed by Sanchez et al. (2005) that define the relationship between task space forces from the controller at the location of the hand, $\mathbf{F}_r$, and the cylinder forces, $\mathbf{f}$, according to

$$\mathbf{F}_r = \mathbf{J}_e^{-\mathrm{T}}\mathbf{J}_c^{\mathrm{T}}\mathbf{f}. \qquad (41)$$

Using this relationship (41) and (12) in the simplified Lyapunov function derivative (40) gives

$$\begin{aligned}\dot{V}(t) &= -\widetilde{\mathbf{x}}^{\mathrm{T}}\boldsymbol{\Lambda}\mathbf{K}_P\widetilde{\mathbf{x}} - \dot{\widetilde{\mathbf{x}}}^{\mathrm{T}}\mathbf{K}_D\dot{\widetilde{\mathbf{x}}} \\ &+ \widetilde{\mathbf{f}}_A^{\mathrm{T}}\left(\boldsymbol{\Psi}\left(\dot{\mathbf{f}}_A - \dot{\mathbf{f}}_A^d\right) + \mathbf{J}_c\mathbf{J}_e^{-1}\mathbf{s}\right) + \widetilde{\mathbf{l}}_A^{\mathrm{T}}\boldsymbol{\Phi}\dot{\widetilde{\mathbf{l}}}_A \\ &+ \widetilde{\mathbf{f}}_B^{\mathrm{T}}\left(\boldsymbol{\Psi}\left(\dot{\mathbf{f}}_B - \dot{\mathbf{f}}_B^d\right) - \mathbf{J}_c\mathbf{J}_e^{-1}\mathbf{s}\right) + \widetilde{\mathbf{l}}_B^{\mathrm{T}}\boldsymbol{\Phi}\dot{\widetilde{\mathbf{l}}}_B. \qquad (42)\end{aligned}$$

We can now substitute the chamber force dynamics (14) and (16) into (42) to obtain

$$\begin{aligned}\dot{V}(t) &= -\widetilde{\mathbf{x}}^{\mathrm{T}}\boldsymbol{\Lambda}\mathbf{K}_P\widetilde{\mathbf{x}} - \dot{\widetilde{\mathbf{x}}}^{\mathrm{T}}\mathbf{K}_D\dot{\widetilde{\mathbf{x}}} \\ &+ \widetilde{\mathbf{f}}_A^{\mathrm{T}}\left(\boldsymbol{\Psi}\left(\mathbf{V}_A^{-1}k(RT\mathbf{A}_A(\dot{\mathbf{m}}_A + \mathbf{l}_A) - \dot{\mathbf{V}}_A\mathbf{f}_A\right) - \dot{\mathbf{f}}_A^d\right) \\ &+ \mathbf{J}_c\mathbf{J}_e^{-1}\mathbf{s}\big) + \widetilde{\mathbf{l}}_A^{\mathrm{T}}\boldsymbol{\Phi}\dot{\widetilde{\mathbf{l}}}_A \\ &+ \widetilde{\mathbf{f}}_B^{\mathrm{T}}\left(\boldsymbol{\Psi}\left(\mathbf{V}_B^{-1}k\left(RT\mathbf{A}_B(\dot{\mathbf{m}}_B + \mathbf{l}_B) - \dot{\mathbf{V}}_B\mathbf{f}_B\right) - \dot{\mathbf{f}}_B^d\right)\right. \\ &- \mathbf{J}_c\mathbf{J}_e^{-1}\mathbf{s}\big) + \widetilde{\mathbf{l}}_B^{\mathrm{T}}\boldsymbol{\Phi}\dot{\widetilde{\mathbf{l}}}_B. \qquad (43)\end{aligned}$$

In addition, we can substitute for the valve leakages $\mathbf{l}_A$ and $\mathbf{l}_B$ (34) into (43) to obtain

$$\begin{aligned}\dot{V}(t) &= -\widetilde{\mathbf{x}}^{\mathrm{T}}\boldsymbol{\Lambda}\mathbf{K}_P\widetilde{\mathbf{x}} - \dot{\widetilde{\mathbf{x}}}^{\mathrm{T}}\mathbf{K}_D\dot{\widetilde{\mathbf{x}}} \\ &+ \widetilde{\mathbf{f}}_A^{\mathrm{T}}\left(\boldsymbol{\Psi}\left(\mathbf{V}_A^{-1}k\left(RT\mathbf{A}_A\left(\dot{\mathbf{m}}_A + \widehat{\mathbf{l}}_A\right) - \dot{\mathbf{V}}_A\mathbf{f}_A\right) - \dot{\mathbf{f}}_A^d\right)\right. \\ &+ \mathbf{J}_c\mathbf{J}_e^{-1}\mathbf{s}\big) + \widetilde{\mathbf{l}}_A^{\mathrm{T}}\left(\boldsymbol{\Phi}\dot{\widetilde{\mathbf{l}}}_A - kRT\mathbf{A}_A\mathbf{V}_A^{-1}\boldsymbol{\Psi}\widetilde{\mathbf{f}}_A\right) \\ &+ \widetilde{\mathbf{f}}_B^{\mathrm{T}}\left(\boldsymbol{\Psi}\left(\mathbf{V}_B^{-1}k\left(RT\mathbf{A}_B\left(\dot{\mathbf{m}}_B + \widehat{\mathbf{l}}_B\right) - \dot{\mathbf{V}}_B\mathbf{f}_B\right) - \dot{\mathbf{f}}_B^d\right)\right. \\ &- \mathbf{J}_c\mathbf{J}_e^{-1}\mathbf{s}\big) + \widetilde{\mathbf{l}}_B^{\mathrm{T}}\left(\boldsymbol{\Phi}\dot{\widetilde{\mathbf{l}}}_B - kRT\mathbf{A}_B\mathbf{V}_B^{-1}\boldsymbol{\Psi}\widetilde{\mathbf{f}}_B\right). \qquad (44)\end{aligned}$$

Next, we use mass flow control laws of (17) and the leakage estimate update laws of (18) in (44) in order to obtain

$$\dot{V}(t) = -\widetilde{\mathbf{x}}^{\mathrm{T}}\boldsymbol{\Lambda}\mathbf{K}_P\widetilde{\mathbf{x}} - \dot{\widetilde{\mathbf{x}}}^{\mathrm{T}}\mathbf{K}_D\dot{\widetilde{\mathbf{x}}} - \widetilde{\mathbf{f}}_A^{\mathrm{T}}\boldsymbol{\Omega}\widetilde{\mathbf{f}}_A - \widetilde{\mathbf{f}}_B^{\mathrm{T}}\boldsymbol{\Omega}\widetilde{\mathbf{f}}_B. \qquad (45)$$

This result shows global asymptotic stability for the controlled system for a system with dynamics defined by (1), (14) and (16). Although (45) proves stability for any choice of positive-definite gain matrices, in practice, un-modeled structural dynamics, un-modeled flow dynamics, plumbing flow restrictions, and discrete-time approximations limit the stability of the system. This reduces the magnitude of acceptable values for the controller gains. However, with some gain tuning, the experimental results demonstrate that good performance can be achieved.

References

Al-Dakkan, K. A. et al. (2003). Energy saving control for pneumatic servo systems. *Proceedings 2003 IEEE/ASME International Conference on Advanced Intelligent Mechatronics, 2003 (AIM 2003).*

Bobrow, J. E. and McDonell, B. W. (1998). Modeling, identification, and control of a pneumatically actuated, force controllable robot. *IEEE Transactions on Robotics and Automation*, **14**(5): 732–742.

Fite, K. B. et al. (2006). A unified force controller for a proportional-injector direct-injection monopropellant-powered actuator. *Journal of Dynamic Systems, Measurement, and Control*, **128**: 159.

Granosik, G. and Borenstein, J. (2004). Minimizing air consumption of pneumatic actuators in mobile robots. *Proceedings 2004 IEEE International Conference on Robotics and Automation, 2004 (ICRA'04).*

He, J. et al. (2005). RUPERT: a device for robotic upper extremity repetitive therapy. *27th Annual International Conference of the Engineering in Medicine and Biology Society, 2005 (IEEE-EMBS 2005)*, 6844–6847.

Leavitt, J. et al. (2006). High bandwidth tilt measurement using low cost sensors. *IEEE/ASME Transactions on Mechatronics*, **11**(3): 320–327.

Murray, R. M. et al. (1994). *A Mathematical Introduction to Robotic Manipulation.* CRC Press, Boca Raton, FL.

Rahman, T. et al. (2004). Design and testing of WREX. *Lecture Notes in Control and Information Sciences*, pp. 243–250.

Reinkensmeyer, D. J. et al. (2006). Tools for understanding and optimizing robotic gait training. *Journal of Rehabilitation Research and Development*, **43**(5): 657–670.

Richer, E. and Hurmuzlu, Y. (2000a). A high performance pneumatic force actuator system: part I—Nonlinear mathematical model. *Journal of Dynamic Systems, Measurement, and Control*, **122**: 416.

Richer, E. and Hurmuzlu, Y. (2000b). A high performance pneumatic force actuator system: part II—Nonlinear controller design. *Journal of Dynamic Systems, Measurement, and Control*, **122**: 426.

Sanchez, R. J. et al. (2005). A pneumatic robot for re-training arm movement after stroke: Rationale and mechanical design. *9th International Conference on Rehabilitation Robotics, 2005 (ICORR 2005)*, pp. 500–504.

Sanville, F. E. (1971). A new method of specifying the flow capacity of pneumatic fluid power valves. *Hydraulic Pneumatic Power*, **17**: 195.

Shearer, J. L. (1956). Study of pneumatic processes in the continuous control of motion with compressed air. *Transactions of the ASME*, **78**: 233–249.

Slotine, J. J. E. and Li, W. (1991). *Applied Nonlinear Control*. Prentice-Hall, Englewood Cliffs, NJ.

Surgenor, B. W. and Vaughan, N. D. (1997). Continuous sliding mode control of a pneumatic actuator. *Journal of Dynamic Systems, Measurement, and Control*, **119**(3): 578–581.

Wolbrecht, E. T. et al. (2006). Control of a pneumatic orthosis for upper extremity stroke rehabilitation. *28th Annual International Conference of the IEEE Engineering in Medicine and Biology Society, 2006 (EMBS '06)*, New York.

Wolbrecht, E. T. et al. (2008). Optimizing compliant, model-based robotic assistance to promote neurorehabilitation. *IEEE Transactions on Neural Systems and Rehabilitation Engineering*, **16**(3): 286–297.

Xiang, F. and Wikander, J. (2004). Block-oriented approximate feedback linearization for control of pneumatic actuator system. *Control Engineering Practice*, **12**(4): 387–399.